Supplementary material: Renormalization group analysis of competing quantum phases in the J_1-J_2 Heisenberg model on the kagome lattice

Raik Suttner, Christian Platt, Johannes Reuther, and Ronny Thomale

PSEUDOFERMION FUNCTIONAL RENORMALIZATION GROUP

In this section we elaborate on various technical details of the pseudofermion functional renormalization group method, which we apply to map out the phase diagram of the KHM. As mentioned in the paper, we first express the spin operators in terms of pseudofermions, using the representation $S^\mu = 1/2 \sum_{\alpha\beta} f^\dagger_\alpha \sigma^\mu_{\alpha\beta} f_\beta$, ($\alpha, \beta = \uparrow, \downarrow$, $\mu = x, y, z$) with fermionic operators $f_\uparrow$ and $f_\downarrow$ and Pauli-matrices σ^μ. The introduction of pseudofermions leads to an artificial enlargement of the Hilbert space and therefore requires the fulfillment of an occupancy constraint, excluding empty and doubly occupied states. Since an unphysical occupation acts as a vacancy in the spin lattice associated with an excitation energy on the order of the exchange coupling, particle number fluctuations are suppressed at zero temperature such that the constraint is naturally fulfilled in the ground state. The fermionic representation allows one to apply standard diagrammatic many-body techniques. In particular, the free propagator in Matsubara-space is simply given by $G_0(i\omega) = \frac{1}{i\omega}$, where due to the absence of quadratic terms in the fermionic Hamiltonian, $G_0(i\omega)$ does not contain any self-energy contributions. As a consequence of this property, the propagator is strictly local in real space.

The FRG procedure first amounts to introducing an infrared frequency cutoff in the propagator, replacing $G_0(i\omega) \to G_0^\Lambda(i\omega) = \frac{\Theta(|\omega|-\Lambda)}{i\omega}$. Here, we use a sharp cutoff implemented by a Θ-function, however, the FRG does not rely on this particular choice. As a consequence of this replacement, all m-particle vertex functions acquire a Λ-dependence, which is described by the FRG flow equations. A schematic form of these equations is shown in Figs. 4a and 4b. The flow of the self energy (Fig. 4a) couples to itself (via fully dressed propagators) and to the two-particle vertex. In turn, the flow of the two-particle vertex (Fig. 4b) couples to the self energy, to itself and to the three-particle vertex. This way the FRG generates an infinite hierarchy of coupled RG equations for all m-particle vertices. For an actual solution, a truncation procedure needs to be performed. While for most FRG applications, it is sufficient to neglect the three-particle vertex completely, here we keep certain three-particle contributions as indicated in Fig. 4c. This truncation leads to a better fulfillment of Ward-identities [1] and, moreover, ensures that via better feedback of the self energy into the two-particle vertex flow, spin-mean field as well as RVB-mean field limits are included in an entirely self-consistent way. Magnetic ordering tendencies and quantum fluctuations can, hence, be described within the same RG framework. The spin susceptibility, which is the central quantity to be investigated in the pseudofermion FRG, can be computed by fusing the external legs of the two-particle vertex, see Fig. 4d. The RG flow starts in the limit $\Lambda \to \infty$ where the two-particle vertex is given by the bare interaction $\sim J$ and ends at $\Lambda = 0$ when the cutoff is completely removed.

The RG equations in Fig. 4 are solved in the frequency domain (keeping all frequency dependencies of the vertex functions) and in real space. For a finite set of differential equations the frequency dependencies need to be discretized, typically by choosing a logarithmic mesh of discrete frequency points. Furthermore, the real space dependence needs to be truncated. While formally, we treat the system as an infinite lattice and exploit translation invariance, spin-spin correlations (i.e., two-particle vertices) are only taken into account up to maximal length. Consequently, the *effective* system size, i.e., the area in which all spins are correlated among each other, becomes finite (in our studies up to 317 lattice sites).

CLASSICAL PHASE DIAGRAM

In the following, we discuss the classical J_1-J_2 KHM [2, 3] as obtained in the large-spin limit in more detail. Fig. 5 shows the corresponding phase diagram comprising $\mathbf{q} = 0$ order, cuboc order, ferromagnetic order, and $\sqrt{3} \times \sqrt{3}$ order. All phase boundaries coincide either with the J_1 or the J_2 axis, except for the transition between the cuboc and the ferromagnetic phase, which lies at $J_2 = -J_1/3$. The peak structures of the Fourier transforms of these types of order are also shown in Fig. 5. We emphasize that Fourier transformed quantities on the Kagome lattice have the periodicity of the second (extended) Brillouin zone, indicated by black hexagons in Fig. 5. Unlike the cuboc and $\mathbf{q} = 0$ order, the ferromagnetic and $\sqrt{3} \times \sqrt{3}$ order cannot be decomposed into harmonics with equal wave vectors $|\boldsymbol{k}|$. These types of order require two inequivalent harmonics.

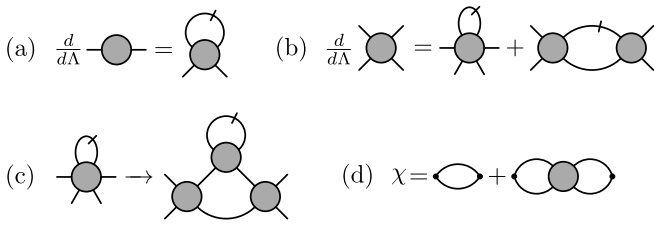

FIG. 4. Diagrammatic representation of the FRG equations. Lines denote fully dressed propagators, slashes are derivatives ∂_Λ. Eqs. (a) and (b) are the FRG equations for the self-energy and the two-particle vertex, respectively (without distinguishing between the different interaction channels on the right side of (b)). The truncation scheme is illustrated by the replacement (c). The magnetic susceptibility is obtained by fusing the external legs of the two-particle vertex, as shown in (d).

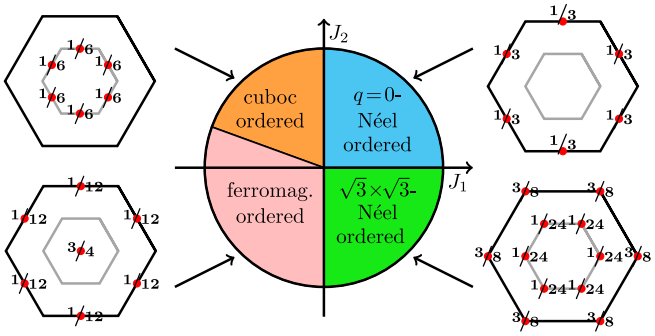

FIG. 5. The phase diagram of the classical J_1-J_2 KHM with $\mathbf{q} = 0$ order, cuboc order, ferromagnetic order, and $\sqrt{3} \times \sqrt{3}$ order, see also Ref 3. The left and right sides of the figure show the $\boldsymbol{k}$-space positions of the classical ordering peaks corresponding to these types of order (red dots). The black (gray) hexagons represent the boundaries of the second (first) Brillouin zone. Numbers indicate the relative peak heights of the different ordering peaks, which always add up to one within the second Brillouin zone.

DIMER CORRELATIONS

In order to investigate the properties of the magnetically disordered regimes of the quantum J_1-J_2 KHM we have probed the system with respect to its propensity to form various dimerized VBCs. By definition, a VBC is a periodic arrangement of dimer bonds on pairs of nearest neighbor sites (i, j), such that each site belongs to exactly *one* dimer. In the following, for a given configuration, S denotes the set of all such pairs of sites while W is the set of all other nearest neighbor bonds. Within our FRG framework, a conceptually simple way to calculate generalized dimer susceptibilities χ^{dimer}, measuring the tendency of the system to support a specific VBC, is to add a small perturbation H_{D} to the Hamiltonian,

$$H_{\text{D}} = \delta \sum_{(i,j)\in S} \mathbf{S}_i \mathbf{S}_j - \delta \sum_{(i,j)\in W} \mathbf{S}_i \mathbf{S}_j \,, \qquad (1)$$

which strengthens the couplings J_{ij} on all dimer bonds in S [$J_{ij} \to J_{ij} + \delta$ if $(i, j) \in S$] and weakens all other nearest neighbor couplings [$J_{ij} \to J_{ij} - \delta$ if $(i, j) \in W$], see also Refs. 4 and 5. Such a modification affects the initial conditions of the RG flow at large cutoff scales Λ. As Λ is lowered, we keep track of the evolution of all static nearest neighbor spin-spin correlations $\chi_{ij} = \langle\langle \mathbf{S}_i \mathbf{S}_j \rangle\rangle(\omega = 0)$. We then define the dimer susceptibility for a given pair of adjacent sites (i, j) by $\chi_{ij}^{\text{dimer}} = -(\chi_{ij} - \chi_m)/\delta$ where χ_m is a properly chosen mean value over all nearest neighbor bonds (see below). If the absolute value $|\chi_{ij}^{\text{dimer}}|$ is small, the system tends to equalize (i.e. reject) the perturbation on that link, while a large value indicates that the system supports the dimerization. In Figs. 3 and 6, $|\chi_{ij}^{\text{dimer}}|$ is encoded in the thickness of the lines connecting nearest neighbor bonds. Furthermore, the color (green, red) indicates the sign of χ_{ij}^{dimer} which distinguishes between weakened and strengthened bonds.

For the HVBC introduced in the paper, as well as for most of the other patterns that we have tested, the unit cell consists of 6 inequivalent strengthened nearest neighbor bonds with $(i, j) \in S$ and 18 inequivalent weakened nearest neighbor bonds with $(i, j) \in W$. It is convenient to define the mean value of the spin-spin correlations by

$$\chi_m = \left(\sum_{(i,j)\in S} 3\chi_{ij} + \sum_{(i,j)\in W} \chi_{ij} \right) /36 \,, \qquad (2)$$

where the sums only run over inequivalent links in a unit cell. In Eq. (2) the strengthened bonds contribute with an additional factor of 3. This ensures that in total strengthened and weakened bonds are equally weighted such that at the beginning of the RG flow (i.e., at large Λ) $|\chi_{ij}^{\text{dimer}}|$ is constant on all bonds (left-hand pictures in Figs. 3 and 6). In general, not only the Λ-evolution of the magnitude of the dimer susceptibilities $|\chi_{ij}^{\text{dimer}}|$ is relevant but also their spatial homogeneity: The formation of a VBC is indicated by a large *and* homogeneous dimer response. On the other hand, an inhomogeneous response shows that certain bonds might have a bias towards dimerization while the dimer pattern as a whole is rejected and long-range order does not develop. Furthermore, the existence of long range dimer-order implies that the magnitude of responses differs significantly between the pattern which is supported by the system and slightly modified patterns.

In the main text, we have discussed the HVBC [6] as well as a modified pattern (Fig. 3). While the central pinwheel structure gains considerable weight during the RG flow, the overall response is rather inhomogeneous. Keeping the 36 site unit cell and the pinwheel, there exists another related pattern, which we have also tested, see Fig. 6a. The susceptibility distribution shows the same degree of inhomogeneity as compared to Fig. 3. Note that as in Fig. 3, the corners of the unit cell in Fig. 6a exhibit a local dimer arrangement which has been re-

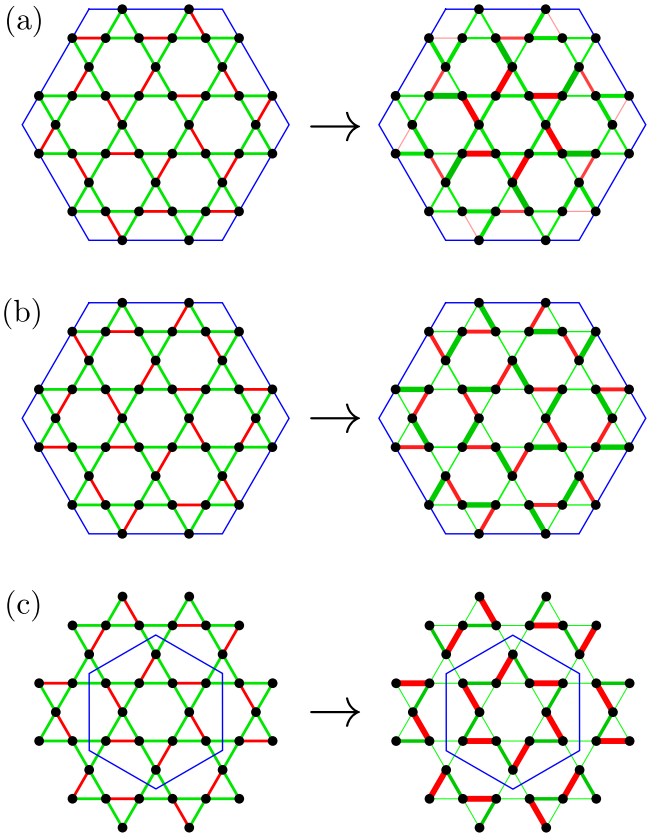

FIG. 6. Further valence-bond configurations that we have studied. Again, red lines correspond to strengthened and green lines to weakened bonds. Blue lines mark the unit cell boundaries (note the smaller unit cell in (c)). The pattern in (a) is similar to the valence bond configurations in Fig. 3, i.e., it exhibits "perfect hexagons" at the unit cell corners. (b) represents a pattern of clockwise and counterclockwise rotating pinwheels. A pattern of pinwheels with the same sense of rotation is shown in (c).

ferred to as "perfect hexagon" (i.e. a hexagon with three dimer bonds along its edges). Obviously these features represent the main source of small responses in Figs. 3 and 6a, in agreement with Ref. 7.

Given these results it is interesting to study valence bond configurations which only consist of pinwheels and *no* "perfect hexagons". Fig. 6b shows such a pattern where each strengthened dimer bond belongs to a pinwheel (this is best seen by putting together various unit cells). Together with Figs. 3 and 6a, these four patterns are the only possible valence bond configurations with a 36 site unit cell, a pinwheel structure and (at least) 120° rotation symmetry. Note that as in Fig. 6b, pinwheels have a handedness (clockwise and counterclockwise rotating pinwheels occur in the ratio 1:3). Again, while the pinwheels become the salient features during the RG flow, other bonds exhibit small responses, ruling out long-range order of this type.

Finally, we have tested a dimer pattern which only consists of pinwheels with the same handedness, (Fig. 6c). This gives a unit cell of only 12 sites. The response is very similar to Fig. 6b, in particular, Figs. 6b and 6c show that the "empty triangles" (i.e. the triangles with no dimer bonds along its edges), contribute a very small response signal. This has been noted before [6], as empty triangles are no local eigenstates of the KHM. In total, all patterns that we have tested show similar magnitudes of the responses and also share the same bond inhomogeneities within a patters. This confirms the finding of a low energy scenario involving many competing valence bond configurations.

[1] A. A. Katanin, Phys. Rev. B **70**, 115109 (2004).
[2] M. Spenke and S. Guertler, Phys. Rev. B **86**, 054440 (2012).
[3] J.-C. Domenge, P. Sindzingre, C. Lhuillier, and L. Pierre, Phys. Rev. B **72**, 024433 (2005).
[4] J. Reuther and P. Wölfle, Phys. Rev. B **81**, 144410 (2010).
[5] J. Reuther, D. A. Abanin, and R. Thomale, Phys. Rev. B **84**, 014417 (2011).
[6] R. R. P. Singh and D. A. Huse, Phys. Rev. B **76**, 180407 (2007).
[7] S. Yan, D. A. Huse, and S. R. White, Science **332**, 1173 (2011).